Numerical and analytical simulation of downbursts wind loads

M.T. Chay *[+], F. Albermani[+], R. Wilson[^]
[+]Department of Civil Engineering, University of Queensland, St Lucia Queensland 4072, Australia
[^]Department of Mathematics, University of Queensland, St Lucia Queensland 4072, Australia
*Corresponding Author: email m.chay@uq.edu.au fax+61 7 3365 4599

Abstract

Researchers and designers currently have a number of methods for numerically simulating either the non-turbulent or turbulent characteristics of downbursts. Examples of non-turbulent downburst winds simulated using a commercially available Computational Fluid Dynamics software package are discussed, as well as a simple analytical model. The significance of the translational velocity of the storm, and the variation in intensity as the event matures and decays is discussed. An ARMA method of adding turbulence to the non-turbulent wind speed is proposed. The various aspects of the model are then integrated to create a method suitable for generating wind speed time histories for the dynamic analysis of lattice structures subjected to downburst winds.

Keywords: Thunderstorm, Downburst, Wind, Simulation, Turbulence, Computational Fluid Dynamics, Autoregressive Moving Average Process

1.0 Introduction

Design practices and standards call for wind loads on structures to be evaluated on the basis of an atmospheric boundary layer profile, despite increasing recognition of thunderstorm downbursts as the cause of design wind speeds in many regions of the world. Certainly, downbursts pose a great risk to long span structures, such transmission lines, which undergo regular failures during thunderstorms (Oliver et al 2000)

Researchers have proposed many methods of modelling certain aspects of downburst winds. However, there has been little emphasis on developing a comprehensive model of a downburst that is suitable for the generation of wind loads in a time domain structural dynamic analysis.

The wind of an atmospheric boundary layer can be described as the sum of a mean speed ($\bar{U}(z)$), which is a function of height (z), and a fluctuating process $u'(z,t)$, which is a function of height and time (t).

$$U(z,t) = \overline{U}(z) + u'(z,t) \qquad (1)$$

Similarly, the wind speed occurring at any point in space (x,y,z) and time within a downburst can be thought of as the sum of two vector components:

$$U(x,y,z,t) = \bar{U}(x,y,z,t) + u'(x,y,z,t) \qquad (2)$$

where $U(x,y,z,t)$ is the total wind velocity; $\bar{U}(x,y,z,t)$ is the non-turbulent wind velocity; and $u'(x,y,z,t)$ is the turbulent fluctuation. This form is similar to that of the boundary layer wind, except that now the non-turbulent component is a function of time and location with respect to the storm, and the turbulent component is also affected by the object's relative location to the storm.

This paper discusses methods of modelling several aspects of a downburst and suggests a way in which they may be integrated to produce a model that is able to simulate correlated wind speed time histories at several locations during a storm.

2.0 Non-turbulent downburst models

A number of non-turbulent wind speed models of downbursts are available to engineers. Two methods are presented here: Computational Fluid Dynamics (CFD), and a modified version of an

analytical model originally created for wind shear estimation.

2.1 Computational Fluid Dynamics (CFD)

2.1.1 Validation and Choice of Turbulence Model

CFD modelling techniques have been used previously to investigate a number of characteristics of near ground downburst winds. Selvam and Holmes (1992), and later Wood et al (2001) used a 2-D model to investigate the wind speed increases as downburst winds flowed over a hill. Hangan et al (2003) used a Reynolds stress model to investigate downburst gust front characteristics.

Downbursts are typically simulated as impinging jets, a philosophy which has been adopted in this study. Impinging jet flows are commonplace in today's society, particularly in a variety of manufacturing applications. However, they are particularly difficult to model using CFD, as their flow field is quite complex. As such, impinging jet has been the subject of much scrutiny, and have been widely used as a test case for turbulence models.

During this study, the commercially available CFD package FLUENT 6.0 (Fluent Inc 2003) was used to simulate 30 downburst scenarios with varied diameters and downdraft speeds. The intent in this case was to generate a steady-state model (ie not varying with time) of a non-turbulent downburst wind field, for which time dependency could be later added empirically. The steady-state characteristics of most downburst simulators are often the most studied traits, and generally used for assessing the suitability of an apparatus for simulating such phenomena. While this is a rather simple view of downburst (the variability of downburst strength and size is discussed later in section 2.2.3 of this paper), once simulated, the steady-state flow field presents a simple downburst non-turbulent wind speed 'template' that can be manipulated in a number of computationally efficient ways, which are discussed later, to provide simulated downburst wind speed time histories.

Simulations were performed in three spatial dimensions using a hybrid-tetrahedral mesh. Element size varied throughout the domains used. The smallest elements were located in the impingement zone, and progressively increased in size towards the limits of the domain. A velocity inlet with constant velocity and turbulence intensity was used as the jet outlet and the impingement surface was a 'no slip' wall. Pressure outlets with a zero gauge pressure border the simulation domain. Flow at the velocity inlet was initiated (the velocity inlet was 'turned on') at time t=0. The simulations were run using an unsteady solver, which was computationally more stable than a steady solver, until the flow achieved a steady state.

Unfortunately, there was no suitable full-scale data available for proper validation of the model outputs. In order to validate the CFD simulations, the stationary jet tests (i.e. when the simulated downburst had no translational motion) of the Texas Tech University (TTU) downburst wind tunnel were used as the test case. The wind tunnel utilises a circular jet with an outlet diameter (d_j) of 510mm blowing with an outlet speed (U_{out}) approximately 11m/s, impinging on a flat surface 860mm away from the jet outlet. Full details of this apparatus are available in Chay (2001). The wind field characteristics of this fan forced physical simulation are well documented, and such simulations are accepted as having downburst-like qualities. The philosophy of this approach is that if the CFD model could reproduce the scaled down downburst-like flow of the TTU stationary jet tests, then results would be valid when a full-scale flow is modelled. Figure 1 shows the TTU stationary jet outflow wind speeds (U) as a ratio of U_{out} at a number of heights from the testing surface (z) at several radial distances in the horizontal plane from the centre of the jet (r), otherwise known as the 'centre of divergence'. Dimensions are shown as a ratio of d_j.

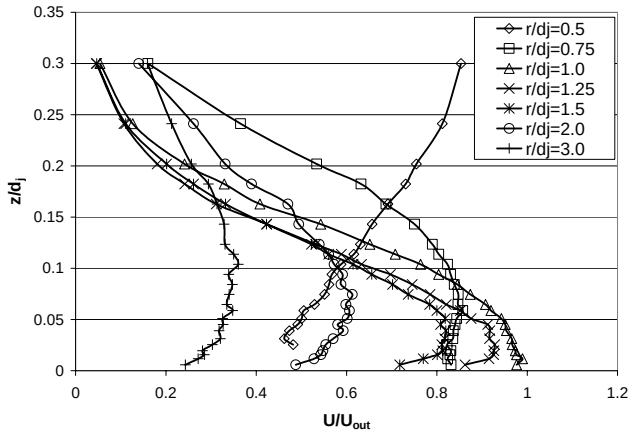

Figure 1: Near-surface wind speed profiles created by the Texas Tech University downburst wind tunnel for a non-translating downburst (Chay and Letchford 2002).

Several of the turbulence models available in FLUENT 6.0 were investigated for the TTU simulations. The models were run using an unsteady simulation from 0 to 4 seconds in 0.05 second increments, with 20 iterations per time step. Jet outlet speed (U_{out}) was 11m/s with 4% turbulence and a hydraulic diameter equal to the jet diameter (d_j=510mm) (Brennan 2004).

The k-ε turbulence models are the most commonly used models, and as such are the best understood and validated of the CFD turbulence simulation methods. They are semi-empirical models based on turbulent kinetic energy (k) and its dissipation (ε).

When modelled in FLUENT 6.0, the exact equation describing ε is approximated. The contribution of fluctuating pressure to dissipation is also neglected, as it is considered negligible in most flows. However, in the stagnation region of an impinging jet, which occurs at small distances from the centre of divergence and close to the impingement surface (approximately r/d_j<0.5 and z/d_j<0.5), it plays an important role in the redistribution of turbulent kinetic energy. There are a number of known shortcomings for the k-ε model when applied to impinging jets. Jing-lei et al (2000) listed two of the major shortcomings as:

- The maximum of the non-turbulent outflow speed is underestimated and it decreases too slowly with increasing r.
- The turbulent kinetic energy production is too high, especially very near the stagnation point at r=0 and z=0, (in which it can be as much as 9 times too large), and the rate of decrease with increasing r is too small.

However, Qing-guan et al (2003) demonstrated that results could be significantly improved by the use of a modified version of the original Renormalization Group (RNG) k-ε model. Several characteristics were considered when assessing the success of the CFD simulations, including the near-ground non-turbulent outflow speed, symmetry of the diverging flow, and non-turbulent wind speed distribution with respect to height. Different turbulence models simulated each of these traits with varying degrees of success. The results presented below were obtained using the RNG k-ε model.

Figure 2 shows a typical wind speed profile comparison of the TTU jet and CFD simulated case at r/d_j =1.0 and r/d_j =1.25. (Note that all CFD data presented for the TTU downburst wind tunnel simulations are for a simulation time of t=4sec).

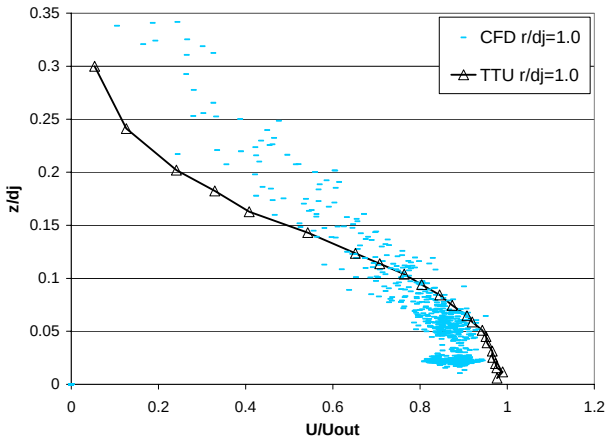

a)

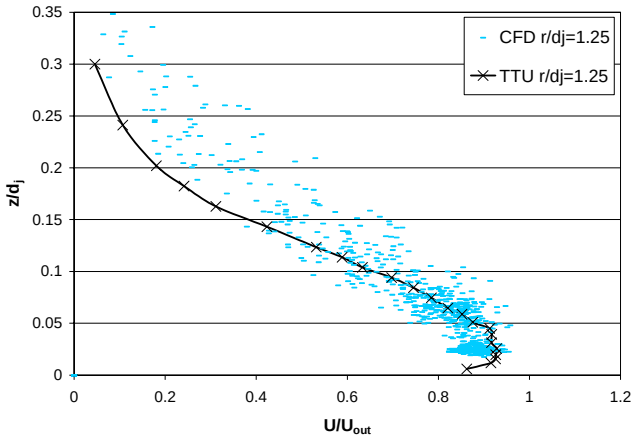

b)

Figure 2: Comparison of wind speed profiles simulated using computational fluid dynamics and full-scale wall jet data at a) r/d_j =1.0 and b) r/d_j =1.25.

Note that due to the irregular nature of the mesh, nodes tended to not occur at exactly the desired distances from the centre of divergence. Therefore, the velocities/turbulence intensities shown as occurring at a fixed radius (for example r/d_j =1.25) occur within a small distance of that radius (in the order of ±2%). The simulated flow field was also not perfectly axisymmetric. Discussion of the flow field asymmetry is given in Section 2.1.3.

The fastest non-turbulent outflow speeds occurred at similar radii in both the measured and simulated flows (in the order of r/d_j=1.0 to r/d_j=1.25). As Figure 2 shows, at r/d_j=1.25 the measured results and simulated wind speeds are very similar. Close to the surface at r/d_j=1.0, the measured TTU flow at a normalised outflow speed of U/U_{out}=0.967 at a normalised elevation of z/d_j =0.0255 whereas the simulated flow produced outflow speeds up to U/U_{out}=0.941 at an elevation of z/d_j=0.0236, and where generally in the order of U/U_{out}=0.9 at that radial distance and height (and as low as U/U_{out}=0.81).

Visually, the CFD simulation reproduces the characteristic shape, or 'velocity nose', of the TTU impinging jet, although the slope of the profile is steeper in the CFD case at higher elevations above surface level, mean that wind speeds in these regions were overestimated.

The primary and secondary ring vortices of a downburst did not occur in the CFD simulations. At the time at which the simulation has stopped, the diverging flow has reached a steady state. While many physical simulations have reported the repeated "pulsing" of regular ground vortices (Cimbala et al 1991, Chay 2001), these do not appear to be present in this method. Figure 3 shows a vector plot of a strip through the centre of the simulation domain. However, as the main 'non-turbulent' flow characteristics of the steady state jet are well represented by the CFD simulation, for the purposes of this study, the absence of the vortices is acceptable.

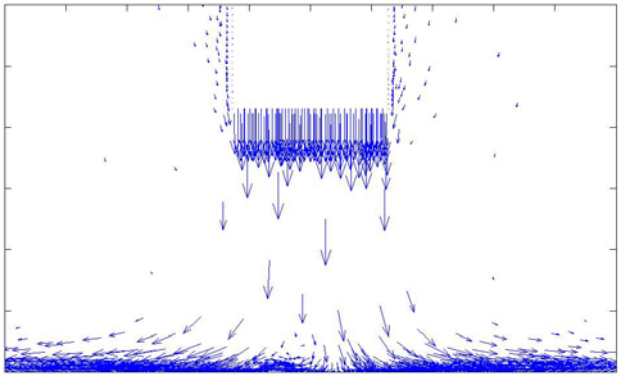

Figure 3: Vector plot taken through a central cross-section of a wind field in a CFD simulation of the TTU moving jet wind tunnel.

The FLUENT 6.0 simulation tended to overestimate the non-turbulent wind speeds at larger radial distances (r/d_j>2.0) and elevations of z/d_j<0.1. However, as the wind speeds at these locations were well below the maximum values, this error was considered to be non-critical.

Based on the observations described above, the CFD simulations were considered to provide an acceptably accurate simulation on the steady state non-turbulent outflow winds of the TTU moving jet wind tunnel, and the RNG k-ε turbulence model was selected for the full-scale simulations.

While the CFD simulations of the non-turbulent wind speeds were successful, turbulence intensity estimates still show large amounts of error. Using the RNG k-ε turbulence model, the turbulence intensity in the CFD simulated TTU flow regime was significantly higher than the measured flow (approximately double), although it was significantly closer to the measured values than the other variants of the k-ε model available in FLUENT 6.0. This is a known shortcoming of these turbulence models and, as an area of future development within the field of Computational Fluid Dynamics, is beyond the scope of this study. A method of applying turbulence to the non-turbulent wind speeds is discussed in section 3 of this paper. Subsequently, further discussion of the CFD turbulence intensity results has been omitted.

A sensitivity analysis was performed to investigate whether accuracy could be improved by introducing the energy equation into the simulation (which is neglected by FLUENT 6.0 as a default), by reducing the time step, or by increasing the number of iterations per time step. There was no significant change in results from these options. Further, running the simulation for a longer duration did not improve accuracy.

2.1.2 Simulation of Full-Scale Events

The first full-scale case considered was a direct scaling of the TTU jet to full-scale. Mason (2003) discussed scales for the facility of:

- Geometry – 3000:1
- Velocity – 3:1
- Time – 1000:1

Subsequently, a jet with z_j=2580m (where z_j is the vertical separation between the jet outlet and impingement surface), d_j=1530m and U_{out}=33m/s was modelled in a 21000m x 21000m x 9750m ($13.725d_j$ x $13.725d_j$ x $6.372d_j$) domain using a mesh with 288645 volumes of varying size, the closest node spacing being 40m. Jet outlet turbulence intensity was kept constant at 4%, and the hydraulic diameter was equal to d_j.

The simulation was then run for 80 time steps of 50 seconds, at which point the outflow had reached a steady state (Note that all CFD results presented are for a simulation time of t=4000 sec). Simulations involved a variety of jet outlet speeds ranging from U_{out}=10m/s to U_{out}=60m/s, to cover a range of surface level speeds that may be reasonably expected to occur and be relevant to a structural investigation. Results at a radial distance of r/d_j=1.0 from the centre of divergence are shown in Figure 4.

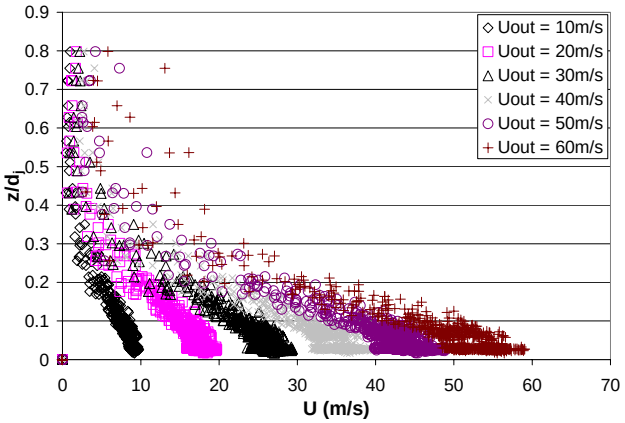

Figure 4: Comparison of wind speed profiles for varied jet outlet speed at r/d_j=1.0.

As anticipated, faster jet speeds produced faster surface level winds. Wind speeds were then non-dimensionalised by the jet speed (Figure 5).

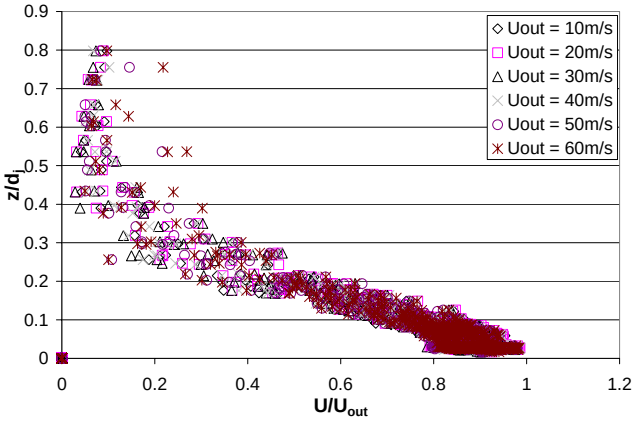

Figure 5: Comparison of wind speed profiles normalized by jet outlet speed at r=1.0d_j.

Figure 5 demonstrates that the non-dimensional outflow wind speed profiles for all the jet outlet speeds are essentially the same. Outflow speed is directly proportional to jet speed in a linear relationship. This is an unexpected result. Wood et al (2001), and later Chay and Letchford (2002) discussed the effect of varying the jet separation from the impingement surface. They found that the non-dimensional outflow wind speed profiles varied in shape as the separation was varied, and that a closer surface produced a higher relative speed (Figure 6). The authors had anticipated that increasing the jet speed would have a similar effect to decreasing the separation between the jet outlet and testing surface. However, the results of the CFD analysis appear to contradict this hypothesis, as Figure 5 fails to show the same trends as Figure 6.

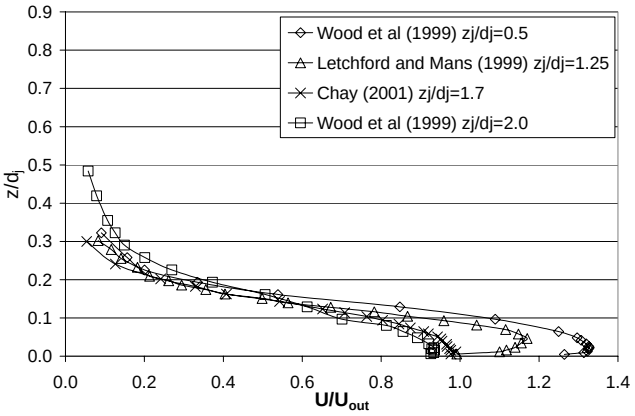

Figure 6: Comparison of wind speed profiles normalized by jet outlet speed with varied jet/impingement surface separation at r/d_j=1.0 for a variety of laboratory wall jets (Chay 2001).

Two new meshes were analysed to determine if FLUENT 6.0 could replicate the results of Wood et al (2001) regarding variation in the outflow regime resulting from a change in z_j. The mesh was the same in every way to the first case, except the jet was positioned at z_j=1500m and z_j=3500m ($0.98d_j$ and $2.29d_j$) above the impingement surface (compared to z_j=2580m, or $1.69d_j$ in the original case). The results are shown in Figure 7.

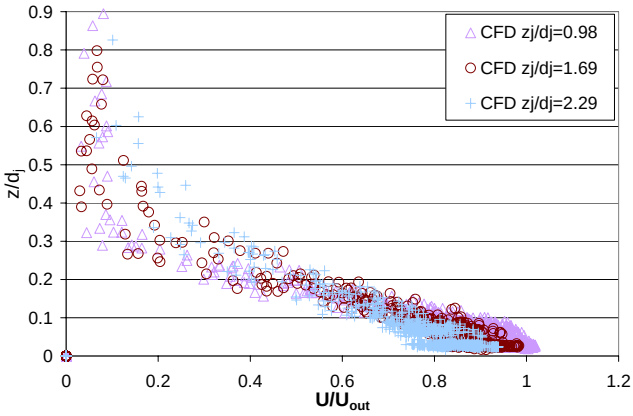

Figure 7: Comparison of wind speed profiles normalized by jet outlet speed with varied jet/impingement surface separation at r/d_j=1.0 for the CFD simulated flows.

While the CFD simulations in Figure 7 exhibited the general trend of decreased jet-surface separation leading to a larger relative outflow speed, the wind speed magnitudes at r/d_j=1.0 did not fit particularly well with the laboratory wall jet data (Figure 6). This is possibly a result of CFD modelling error. As described earlier, k-ε turbulence modelling is known to produce maximum non-turbulent outflow wind speeds that are somewhat lower than the actual values, which would explain the discrepancy in this case.

Four additional jet diameters were also investigated. These were 1000m, 1250mm, 1800m and 2000m. In all cases the jet outlet was 2580m above the impact surface in the same domain size. All other variables were kept the same as the previous series of tests, except for a small amount of variation in the number of mesh volumes, which were generated automatically using the same conditions as were used to generate the previous mesh.

A comparison of results for the different jet diameters at constant outlet speed (in this case 30m/s) is shown in Figure 8. In order to facilitate this comparison, the radius at which the profile is taken is expressed as a ratio of the jet diameter for each case (in this case r/d_j=1.0).

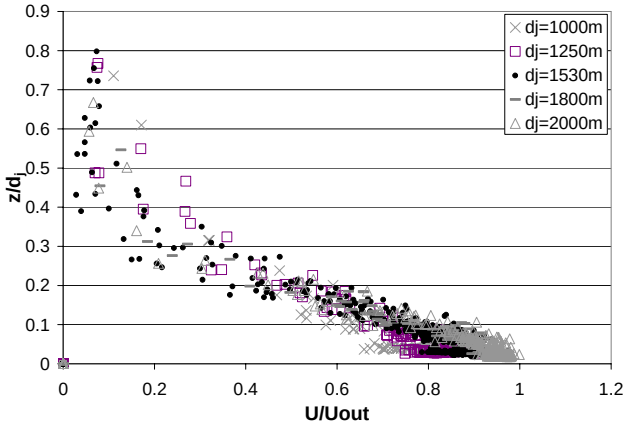

Figure 8: Comparison of wind speed profiles at r/d_j=1.0 and jet outlet speed (U_{out}) 30m/s for varied jet outlet diameters.

Although the profiles are similar, the smaller diameter jets produced lower non-turbulent wind speeds at the same relative position in the outflow. This indicates that while the outflows are comparable in proportion, the flow field does not increase in size in a direct linear relationship with jet diameter, when the jets are positioned a constant distance from impact surface.

This finding is consistent with the results of the comparison in which the jet diameter was held constant, and the distance to the impact surface varied. As the aim of this phase of the model development was to produce a variety of simulated flow fields, the result is useful to the current study. The effect of maintaining a constant jet diameter – jet height ratio was not investigated.

2.1.3 Asymmetry of Results

As mentioned above, the resulting flows from the FLUENT 6.0 downburst simulations were not perfectly axi-symmetric.

The asymmetries in the flow regime appear to be systematically produced by the unavoidable small degree of geometric asymmetry in the mesh. The asymmetry of the flow first becomes apparent in the stagnation region under the jet. Figure 9 shows a plot of the nodal wind vectors in the stagnation region of a CFD simulated downburst (z_j=2580m, U_{out}=33m/s, d_j=1530m). Note that nodes are irregularly spaced, and a 150m wide strip was used. The diverging flow is highly unstable, and these asymmetries have a significant effect as the flow propagates. This occurred in all meshes and all turbulence models. Doubling the resolution of the mesh, beyond which further increase in resolution was not possible due to software/hardware constraints, did not improve the symmetry of the simulation.

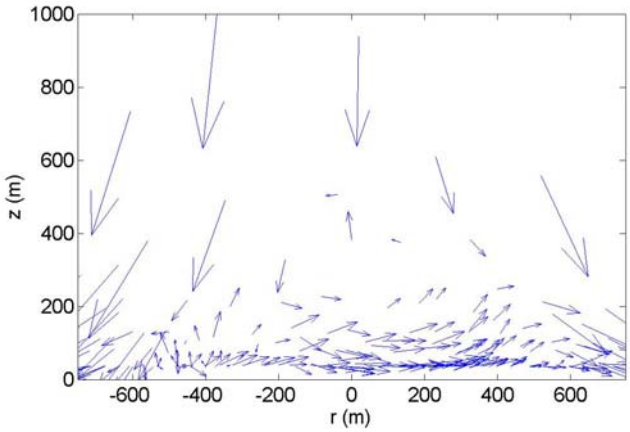

Figure 9: Vector plot of the flow in the stagnation region of a CFD simulated downburst.

Such phenomena have been previously observed in numerical and physical simulations and in full-scale events. Thielen et al (2003) observed asymmetric flow patterns in their CFD simulations of multiple impinging jets even though the initial and boundary conditions and the geometries used were perfectly symmetric. Mason (2003) reported asymmetry in the initial downdraft immediately after a circular jet nozzle was opened, and then observed the gust front to advance in an asymmetric manner (refer Figure 10). Similar traits can be seen in the studies conducted by Landreth and Adrian (1990) and Alahyari and Longmire (1995). These variations likely contain both systematic and random components, but demonstrate the high sensitivity of impinging jet flows to slight asymmetries.

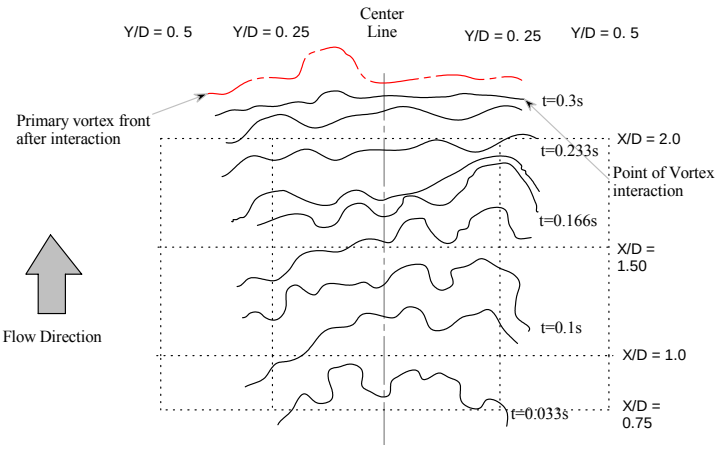

Figure 10: Advance of the primary vortex core of a physically simulated downburst (Mason 2003).

Although somewhat limited in supply, full-scale observations of downbursts also show asymmetry in the diverging wind fields. While a portion of these full-scale asymmetries are likely to be random, one can reasonably expect that a significant part of the variation is due to systematic factors, such as the ambient air conditions or the topography of the ground over which the downburst is flowing. The asymmetric advance of the outflow can be seen in the fine scale radar observations of Lee and Finley (2002).

Wilson et al (1984) quantified the asymmetry of several full-scale cases by determining the ratio of the minimum outflow speed to the maximum outflow speed at fixed radii. They observed an average ratio of approximately 0.4, but quite a deal of variation from case to case. The asymmetries observed during the CFD simulations are within the limits Wilson et al (1984) observed (in the order of 0.8 in the fastest regions of the simulated flow), and are deemed to be acceptable.

2.2 Modified Analytical Model

2.2.1 Original Analytical Model

Oseguera and Bowles (1988), and then later Vicroy (1991), developed an analytical model for the non-turbulent winds of a stationary downburst. The model is axi-symmetric, and does not simulate the ring vortex of the outflow. It is also temporally independent and excludes storm translational velocity. The radial ($\bar{U}_r$) and vertical ($\bar{U}_z$) velocities are given by the equations:

$$\bar{U}_r(r,z) = \frac{\lambda r}{2}\left[e^{c_1(z/z_m)} - e^{c_2(z/z_m)}\right]e^{\left[\frac{2-(r^2/r_p^{\,2})^{\alpha}}{2\alpha}\right]} \qquad (6)$$

$$\bar{U}_z(r,z) = -\lambda\left\{\frac{z_m}{c_1}\left[e^{c_1(z/z_m)}-1\right]-\frac{z_m}{c_2}\left[e^{c_2(z/z_m)}-1\right]\right\}\left[1-\frac{1}{2}\left(\frac{r^2}{r_p^{\,2}}\right)^{\alpha}\right]e^{\left[\frac{2-(r^2/r_p^{\,2})^{\alpha}}{2\alpha}\right]} \qquad (7)$$

where λ is an intensity scaling factor; α, c_1, and c_2 are model constants; r is the radius; r_p is the radius at which the maximum velocity occurs; z is the elevation; and z_m is the elevation at which the maximum wind speed occurs, which is constant for all radii.

Based on recorded full-scale data, Vicroy recommended that c_1 = -0.22 and c_2 = -2.75, although in a later publication (Vicroy 1992) suggested that c_1 = -0.15 and c_2 = -3.2175. Note that the effect of increasing α is to steepen the rate of decay of horizontal winds, and to increase the updraft intensity. Vicroy recommended a value of $\alpha = 2$.

Although the model does not include a ring vortex, the core of this vortex tends to be several hundred metres above ground level (Wilson et al 1984), and the model may therefore be reasonably accurate over the height of a structure.

Chay and Albermani (2004) have suggested several improvements to this model, which can be readily incorporated, and these are discussed below.

2.2.2 Storm Intensity and Height to Maximum Wind Speed

The factor λ (equations (6) and (7)) dictates the strength of the wind field produced. This factor is

quite cumbersome, as changes to r_p or z_m means λ requires recalculation to maintain the same maximum outflow speed. In order to achieve a desired maximum radial speed ($\bar{U}_{r.max}$), λ can be replaced with:

$$\lambda = \frac{2\overline{U}_{r.\max}}{r_p}\left[\frac{1}{e^{\frac{1}{2\alpha}}\left[e^{c_1} - e^{c_2}\right]}\right] \qquad (8)$$

Although the Oseguera and Bowles/Vicroy (OBV) model does attempt to include the effect of friction near the ground, it fails to accurately model boundary layer growth. Wall jet tests (Chay and Letchford 2002) have shown that the thickness of the boundary layer grows as the flow spreads from the centre of divergence, and is also influenced by the relative proximity of the primary and secondary ring vortices in the outflow (Landreth and Adrian 1990). This profile change has also been more recently observed in full-scale (Choi 2004). However, as is shown in Figure 11, the maximum speeds all occur at the same height in the OBV model.

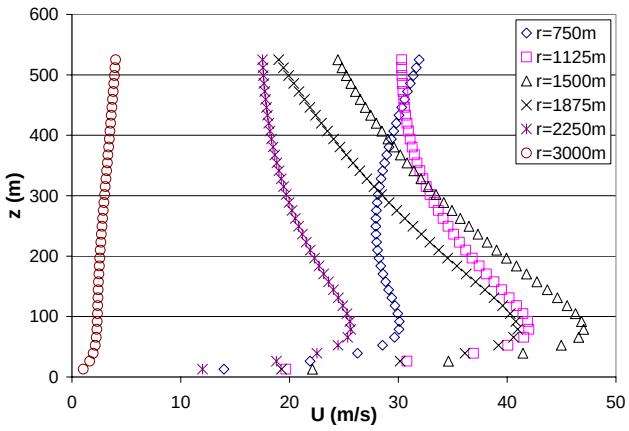

Figure 11: Examples of velocity profiles at varied radius from the centre of divergence (r), for α = 2, r_p = 1500m, z_m = 80m, c_1 = -0.15, c_2 = -3.2174 and λ = 0.595 (Vicroy 1991)

The variation in height at which maximum wind speed occurs can be modelled by exchanging z_m in equations (6) and (7) with z_r, a radially dependent height to maximum wind speed, which is a function of both z_m and r. The vertical wind speeds the OBV model produces are proportional to z_m (which in this new context now represents the height at which the maximum wind speed occurs that corresponds to r_p, meaning that it represents the height of the absolute maximum non-turbulent wind speed in the whole diverging flow field), and would have to be factored down by z_m/z_r.

An accurate relationship between z_r and r is difficult to determine. Boundary layer theory cannot accurately predict the height of the peak in the profile, as the relative proximity of the primary and secondary ring vortices in the outflow heavily influences this attribute. Figure 12 shows an ensemble average of the height of the maximum wind speed (z_r) occurring at a non-dimensional distance from the centre of divergence (r/d_j), normalised by the height at which the absolute peak speed occurred (z_m), for a limited number of wall jet simulations. Note that the ensemble average is calculated only at r/d_j=0.75, 1.0, 1.25, 1.5, 2.0, and 3.0, at which points data was available for all the simulations considered in this case.

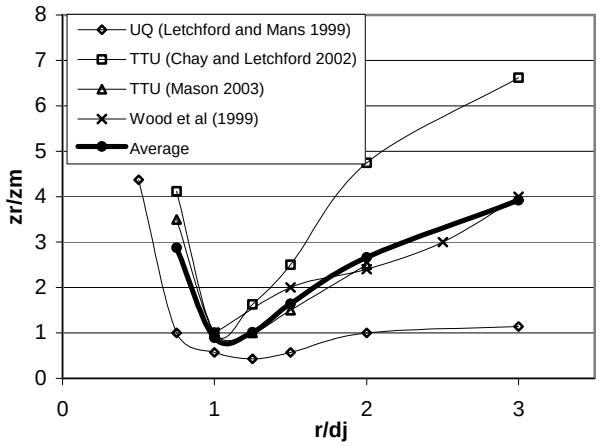

Figure 12: Normalised height of maximum speed (z_r/z_m) versus normalised radius from centre of divergence (r/d_j).

Such data could be used to develop an empirical relationship for z_r and r. However, in the absence of more complete information regarding the vertical and horizontal component of the wind speeds occurring with the wall-jet flows, such a relationship cannot be reliably determined. Separate relationships for z_r may be required for the

radial and vertical wind speed equations. As such, this issue is an area of future research.

2.3 Downburst Flow Regime Variation with Time

The severe winds encountered by a stationary object due to a downburst can last for as little as a few minutes. The relatively brief nature of this kind of an event can be attributed to both its translational movement and variable storm intensity within time and space.

The translational motion causes the flow field of the downburst to progress past a stationary object, subjecting it to varied regions of the flow regime. Further, the downburst winds retain the translational motion of the storm, creating faster winds at the 'front' of the event than those at the 'back' (Letchford and Chay 2002).

Consider an event in which downburst intensity did not vary with time and the storm motion was such that the downburst passed directly over the stationary object, as shown in Figure 13. The building shown would experience highly variable winds, encountering a) weaker, steady winds while it is outside of the downburst flow regime, b) a rapid increase in wind speed as the storm advances to a point at which the object is in the fastest part of the diverging flow regime, c) decreasing winds as the storm advances so that the object is in the stagnation region of the downburst, and d) a 180 swing in wind direction and a secondary peak in wind speed as the storm moves away, before returning to the conditions experience prior to the event. Figure 14 shows that these flow regimes are readily identifiable in an anemometer record taken from Andrews Air Force Base (AAFB) in 1983 (Fujita 1983).

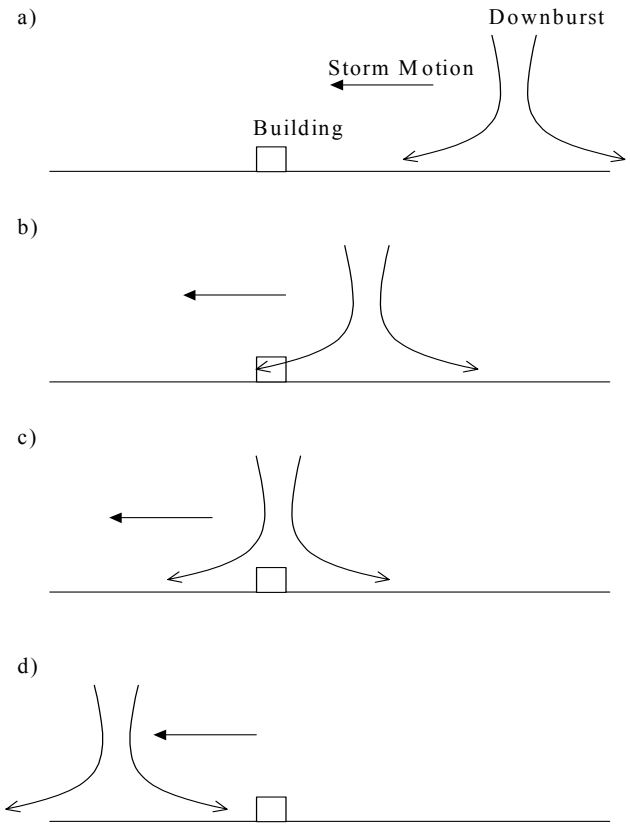

Figure 13: Progression of a downburst over a stationary object.

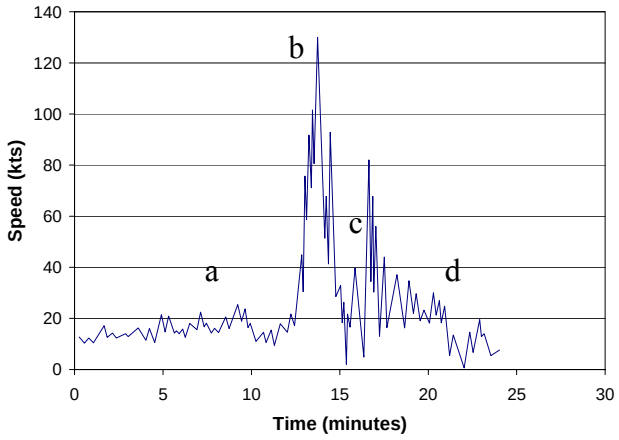

Figure 14: Anemometer trace of a downburst (Fujita 1999)

Holmes and Oliver (2000) developed an empirical model of the non-turbulent downburst wind field. The model is relatively simple, presenting only

horizontal wind speed at a given elevation close to the ground. However, the model includes both the translational speed of the downburst, and a term that simulates the event's decreased intensity with increasing time, attributes which are included in very few other numerical models. The radial wind speed at any time is given by the function:

$$\bar{U}_r(r,t) = \bar{U}_{r,\max}\left(\frac{r}{r_p}\right)e^{(-t/T)} \quad \text{for } r<r_p \tag{9}$$

$$\bar{U}_r(r,t) = \bar{U}_{r,\max}e^{\{-[(r-r_p)/R]^2\}}e^{[-t/T]} \quad \text{for } r\geq r_p \tag{10}$$

where $\bar{U}_r$ is the radial velocity; $\bar{U}_{r,max}$ is the maximum radial velocity; r_p is the radius at which the maximum radial speed occurs; R is a radial length scale; t is the time from when the downburst is at peak intensity; T is a time constant; r is the radial distance from the storm centre, equal to $\sqrt{(x^2+y^2)}$ in a Cartesian reference plane, where x is the horizontal distance from the centre of the storm in the direction of the storms motion at time t, and y is the horizontal distance from the centre of the storm perpendicular to the storms motion at time t

The storm's translation motion ($\vec{U}_{Trans}$) is included in the model through vector summation of the radial and translational velocities. Letchford and Chay's (2002) observations regarding the increase in wind speed associated with a translating wall jet support this method.

The way in which Holmes and Oliver modelled both the translational motion and time-dependent decay of the storm can be readily included in any three dimensional model of the non-turbulent winds of a downburst, such as the CFD simulations or the modified OBV model.

In order for the model to represent the full life of the storm, the time dependency aspect of the model should account for a period of intensification at the start of the event.

Hjelmfelt (1988) reported a period of intensification at the start of downbursts, observing that 5 minutes from the time of first alarm is typically required to reach maximum intensity, although there was a considerable amount of variation between events (Figure 15). Wilson et al (1984) observed that 53% of the downbursts they examined reached maximum velocity within 5 minutes, and 93% within 10 minutes.

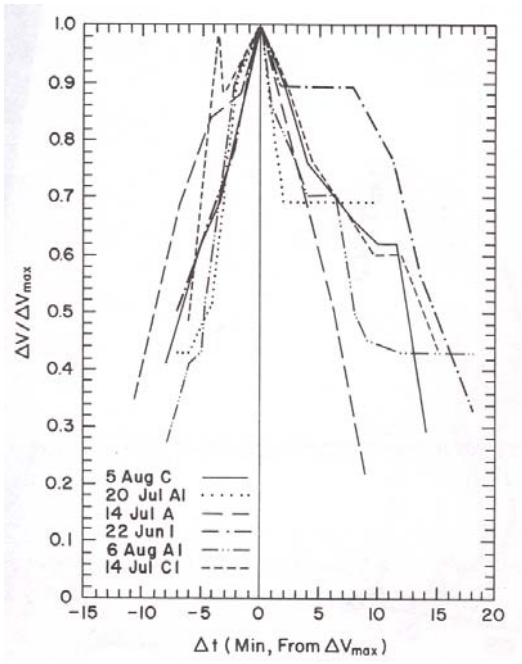

Figure 15: Hjelmfelt's (1988) observations regarding intensity vs time

The radial and vertical wind components of the OBV model can be multiplied by an Intensity Factor (Π) to account for the time dependency of storm strength. As a simple example, consider a 5-minute period of linear intensification from initiation to maximum outflow speed, and then exponential decay afterwards, reaching half strength 8 minutes after maximum intensity. The intensity factor would take the form:

$$\Pi = \begin{cases} \dfrac{t}{5} & 0 \leq t \leq 5 \\ e^{\frac{-(t-5)}{11.542}} & t > 5 \end{cases} \tag{11}$$

where t is time in minutes. Note that a range of relationships could be used here to suit a variety of event types.

Numerical and physical simulations (Lundgren et al 1992; Yao and Lundgren 1996) suggest that during a downburst the radius at which maximum outflow velocity occurs increases with time. Replacing r_p in equations 6 and 7 with a time dependent radius at which the maximum outflow speed occurs (r_t), which is a function of time and r_p, readily accommodates this characteristic. Note that in this new context r_p now represents the radius to maximum outflow speed at Π=1. However, the radial velocity equation in the OBV model has to be reduced by a factor of r_p/r_t, as the original produces radial velocities that are proportional to r_p.

Much more full-scale data is required to accurately determine relationships for z_r, r_t, and Π. However, based on the changes suggested above, the modified OBV model now takes the form:

$$\bar{U}_r(x,y,z,t) = \Pi \frac{\bar{U}_{r.\max} r}{r_t} \frac{\left[e^{c_1(z/z_r)} - e^{c_2(z/z_r)}\right]}{\left[e^{c_1} - e^{c_2}\right]} e^{\left[\frac{1-(r^2/r_t^2)^\alpha}{2\alpha}\right]} + \bar{U}_{Trans} \quad (12)$$

$$\bar{U}_z(x,y,z,t) = -2\Pi \frac{\bar{U}_{r.\max} z_m}{r_t} \frac{\left\{\frac{1}{c_1}\left[e^{c_1(z/z_r)} - 1\right] - \frac{1}{c_2}\left[e^{c_2(z/z_r)} - 1\right]\right\}}{\left[e^{c_1} - e^{c_2}\right]} \left[1 - \frac{1}{2}\left(\frac{r^2}{r_t^2}\right)^\alpha\right] e^{\left[\frac{1-(r^2/r_t^2)^\alpha}{2\alpha}\right]} \quad (13)$$

Note that the non-turbulent wind speeds are now a function of horizontal positions x and y rather than just r, due to the vector summation of the translational velocity of the storm.

The most accurate way to recreate the time varying nature of the downburst flow regime using a CFD simulation would be to examine each time step of an unsteady solution between the time at which the downdraft (jet outlet flow) is initiated and the time at which a steady state flow is reached. Although such simulations are well within the capabilities of CFD (Hangan et al 2003), such a procedure would create a dataset that was excessively large, and slow to process. As computer technology continues to progress, this will become less of an issue, but at the present time, lends itself to the use of a single, time-independent flow regime template created by the steady-state simulations. While the intensity factor Π can readily be applied to the steady-state flow regime, radial expansion with time cannot, and is an unavoidable shortcoming of using the steady-state data.

3.0 Turbulent fluctuation

There are numerous methods for simulating correlated turbulence with a known spectrum. Of these methods, Auto Regressive Moving Average (ARMA) processes are widely used in time domain dynamic analyses. These methods are popular as they are computationally efficient, and after an initial phase of calculation, require only the storage of a set of coefficients and a white noise source. ARMA processes for simultaneously simulating wind turbulence at points in space take the general form:

$$u'(x,y,z,t) = \sum_{i=1}^{q}\left[A_i\right]u'(x,y,z,t-i\Delta t) + \sum_{i=0}^{q}\left[B_i\right]\bar{\Psi}_i \quad (14)$$

where $u'(x,y,z,t)$ is an m-variate vector of the turbulent wind speed at time t, Δt is the size of the discrete time interval at which the time history is generated, $[A_i]$ and $[B_i]$ are m x m autoregressive and moving average coefficient matrices, respectively, for i time steps prior to t, Ψ_i is an m-variate Gaussian white noise series, and m is the number of points in space. Each component of $u'(x,y,z,t)$ corresponds to a nodal point in space in the Cartesian plane. The location of the nodes relative to the storm varies with time due to the translational movement of the storm. Note that in this case, equal orders (q) for the autoregressive and moving average components have been assumed.

Samaras et al (1985) suggested a similar method that generated a correlated Gaussian noise source with zero mean and unit variance. The output can then be readily converted to a wind time history by

multiplying by an appropriate factor to create the desired variance, and adding the mean speed at all locations.

Note that the spectra and coherences used in ARMA wind turbulence simulations are not truly 'stationary' as they are dependent on absolute elevation (z), rather than relative elevation (Δz). However, they are representative of the actual nature of the process being simulated, and despite this non-stationarity, can still be simulated using the ARMA method described. A verfication study was performed in which a series of simultaneously generated time histories were created for an array of locations using the Kaimal spectrum (Kaimal et al 1972) and Davenport's approximation for coherence (Simiu and Scanlan 1996). Temporal and spatial correlations were back-calculated from the simulated time histories, and in all cases the results matched the theoretical inputs.

As there is insufficient full-scale data to accurately describe the coherence in downburst winds, it has been assumed that Davenport's coherence for boundary layer winds can be used. The accuracy of this assumption remains an area of future research, and requires closer investigation as more full-scale data becomes available.

Unfortunately, ARMA processes become unstable as the time step is reduced. The ARMA process is based upon the covariance structure for a continuous time process. Consequently, as the time increments are reduced, the orders required for the ARMA process to provide a good approximation may vary considerably and are difficult to predict, leading to instability. Note that an ARMA process with order (4,4) was able to successfully simulated wind turbulence at 5Hz in this case. To apply this method to the dynamic analysis of a non-linear structure (which requires quite a small time step) it may be necessary to interpolate between times at which the wind speeds are generated. Interpolation introduces a degree of statistical non-stationarity into the simulated time history, as the probability distribution of the interpolated points will be different to that of the simulated points. However, with appropriate parameter choice, the effect of this interpolation is very small.

Chen and Letchford (2004a) presented a method of combining turbulence with a non-turbulent downburst wind field based on an Evolutionary Power Spectral Density method. The EPSD is used to generate a correlated Gaussian stochastic process, $\kappa(x,y,z,t)$ with zero mean and unit variance. The wind speed fluctuation is obtained by amplitude modulating the process:

$$u'(t) = a(x,y,z,t)\kappa(x,y,z,t) \tag{15}$$

$a(x,y,z,t)$ is the amplitude modulation factor, equal to:

$$a(x,y,z,t) = 0.25\overline{U}(x,y,z,t) \tag{16}$$

where $\overline{U}(x,y,z,t)$ is the non-turbulent wind speed.

However, in a later document (Chen and Letchford 2004b), they suggest that $a(x,y,z,t)$ be equal to between 0.08 and 0.11 times the non-turbulent wind speed:

$$a(x,y,z,t) = 0.08\overline{U}(x,y,z,t) \text{ to } a(x,y,z,t) = 0.11\overline{U}(x,y,z,t) \tag{17}$$

The Chen and Letchford amplitude modulation method can be readily combined with the Samaras et al method of ARMA turbulence generation. The unit variance Gaussian process $\kappa(x,y,z,t)$ is generated separately, using Samaras et al's method, taking the form:

$$\kappa(x,y,z,t) = \sum_{i=1}^{q}\left[A_i\right]\kappa(x,y,z,t-i\Delta t) + \sum_{i=0}^{q}\left[B_i\right]\bar{\Psi}_i \tag{18}$$

A value of q=4 has been used throughout this paper. The turbulent fluctuations can then be amplitude modulated to the appropriate intensity as per (15). This method is summarised in Appendix A.

The form of the factor *a(x,y,z,t)* is still debatable. When applied to a stationary non-turbulent velocity, equation (16) yields a turbulence intensity of 25% at all parts of the regime. Chen and Letchford's (2004b) analysis of full-scale wind speed time histories supports the use of constant turbulence intensity.

However, Chang and Frost (1987) reported full-scale turbulence intensities that varied as a function of radius and height (see Figure 16).

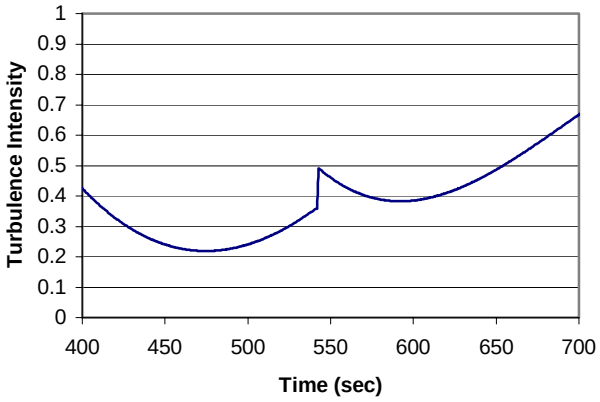

Figure 16: Turbulence intensity experienced by an object traversing the downburst wind field at U_{trans}=12m/s in the positive y direction and initial coordinates of x=10m, y=6500m, and z=30m

Note that there is a discontinuity in the turbulence intensity profile. This occurs as the object moves from one quadrant of the flow to another. This is an obvious flaw, but could be overcome by interpolation. The location of the object relative to the storm could be expressed in cylindrical coordinates. If turbulence intensity was calculated at the local North, South, East and West axes (forward, backwards, right and left relative to the motion of the storm, respectively), then interpolation along a radial line can be used to calculate turbulence intensity at any point between these axes for a given radius.

Unfortunately, both Chen and Letchford's and Chang and Frost's observations are based on very limited data sets. However, Chang and Frost's observations were based on radar derived estimates and recordings from aircraft traversing the downburst. Chen and Letchford's data was recorded using a network of instrumented towers, and as such recorded data under conditions for which this model is intended to simulate downbursts. Therefore, while still requiring much greater full-scale data for validation, constant turbulence intensity is considered to be correct for this study.

4.0 Case Study

4.1 Single Point Time Histories

The first case considered is the output of the original OBV model (equations 6 and 7). The model excludes any time dependency on translational speed. The object in question had an initial location of 6500m from the storm, an elevation of 40m, and traversed at 12m/s through a path 10m off centre of the storm. The model was configured with r_p=1500m, z_m=80m, and λ=0.03796. Turbulent fluctuations were created using the Samaras et al method (1985), and the fluctuations were modulated using the Chen and Letchford (2004a) method and a value of $a(x,y,z,t) = 0.1\,\overline{U}(x,y,z,t)$. The results are shown in Figure 17. Note that only wind speed is shown in this case (not direction).

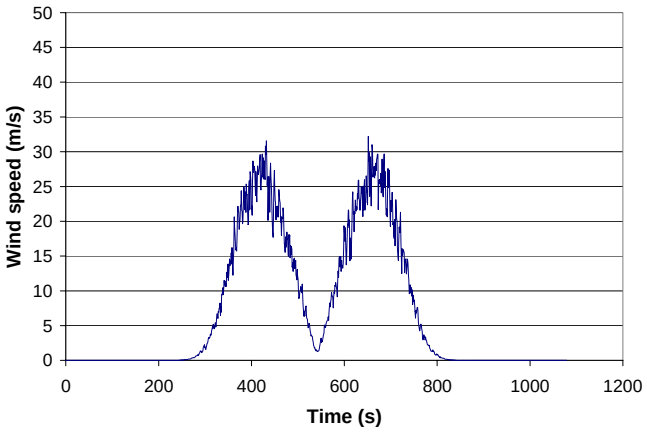

Figure 17: Wind speed time history generated using the basic OBV non-turbulent wind speed model

Adopting the analytical model in this form provides a relatively poor downburst simulation.

The modified analytical model was used to create simulations for two scenarios: one in which the intensity factor is of the form described by (11) (Figure 18), and one in which the storm remains at full strength after the initial intensification period (Figure 19). The storm is configured to have similar properties to that modelled in Figure 17 (r_p=1500, U_{max}=30, U_{trans}=12m/s). For these scenarios, z_m was held constant at 80m. In both cases r_t increases linearly from 1000m at the start of the event to 1500m after 5 minutes and continues to grow linearly for the remainder of the event.

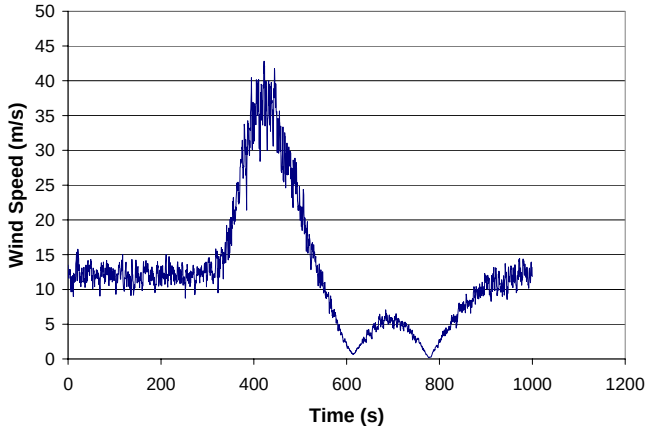

Figure 18: Wind speed time history generated using the modified OBV model to estimate non-turbulent wind speed.

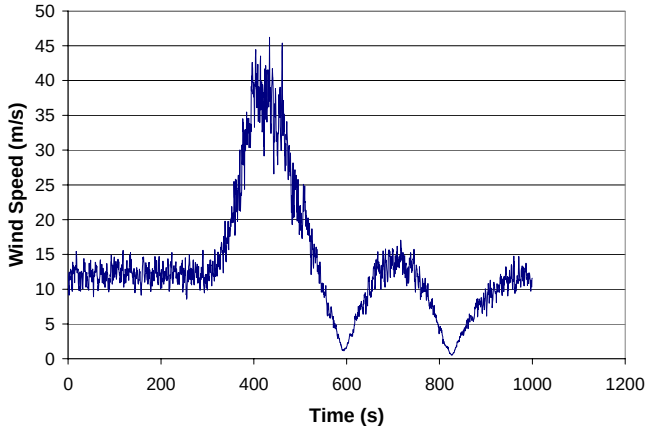

Figure 19: Wind speed time history generated using the modified OBV model to estimate non-turbulent wind speed, maintaining full storm intensity.

The modifications to the analytical model clearly improve the form of the simulation. The effect of varying the intensity factor as described above modifies the size of the rear flank secondary peak (the region 'd' flow described in Figure 13). Obviously, the storm which did not decline in intensity after reaching peak strength had larger wind speeds in the secondary peak, which was also more prolonged.

Figure 20 shows the results of a simulation in which a RNG k-ε CFD simulated downburst with a jet diameter of 1530m, and an exit velocity of 33m/s provided the non-turbulent wind speed. The non-turbulent wind speeds are provided by the steady-state flow regime at t=4000 sec after the downdraft was initiated at the jet outlet (z_J=2580m). An intensity factor as described by (11) was applied to the flow.

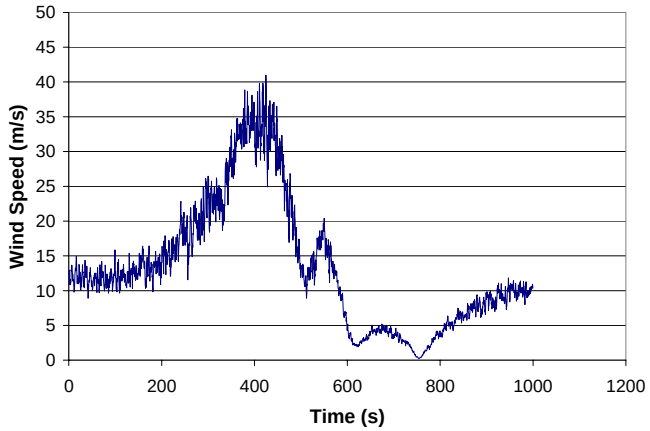

Figure 20: Wind speed time history generated using a CFD simulated non-turbulent wind

The CFD simulation produces a slower rate of wind speed increase at the beginning of the event. This was to be expected. The analytical model recreates a strong gust front at the edge of the event, whereas the CFD simulation was of a steady-state jet, for which the gust front has advanced beyond the limits of the simulation.

The time dependant model was used to recreate the AAFB microburst anemometer record (Figure 21).

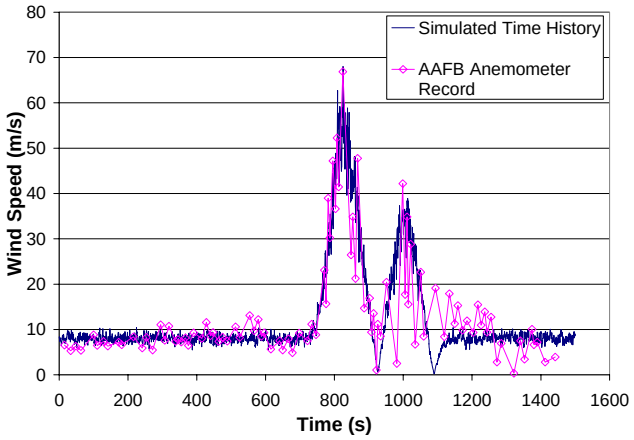

Figure 21: Comparison of simulated and recorded wind speed records.

The event was simulated using U_{max}=120m/s, U_{trans}=8m/s, z_m=80m, $a(x,y,z,t)$ = 0.1, and r_t equal to 700m at the start of the event and increasing linearly at 30m per minute. The intensity factor was given by:

$$\Pi = \begin{cases} \dfrac{t}{2.75} & 0 \le t \le 2.75 \\ e^{\frac{-(t-2.75)}{25}} & t > 2.75 \end{cases} \qquad (19)$$

where time t is in minutes after the start of the event, which was approximately 11 minutes (660s) on the time axis of Figure 21.

Visually, the simulated storm is quite similar to the recorded data. This particular example demonstrates the importance of the intensity factor. Maintaining Π=1 for the full storm would have resulted in an overestimation of the rear flank secondary peak, based on the translational speed. The intensity factor modelled by (19) was approximately equal to 0.88 at the location of the secondary peak, which produced a much better data fit.

4.2 Multiple time histories

Time histories can be generated at numerous points simultaneously based on either method of non-turbulent wind speed simulation presented here (CFD or modified OBV) to form a correlated set of wind speed time histories, which can be readily converted to a set of correlated loading time histories for the dynamic analysis of a structure.

Figure 22 shows a set of simultaneous time histories for nodes at 20m lateral spacing for the AAFB case.

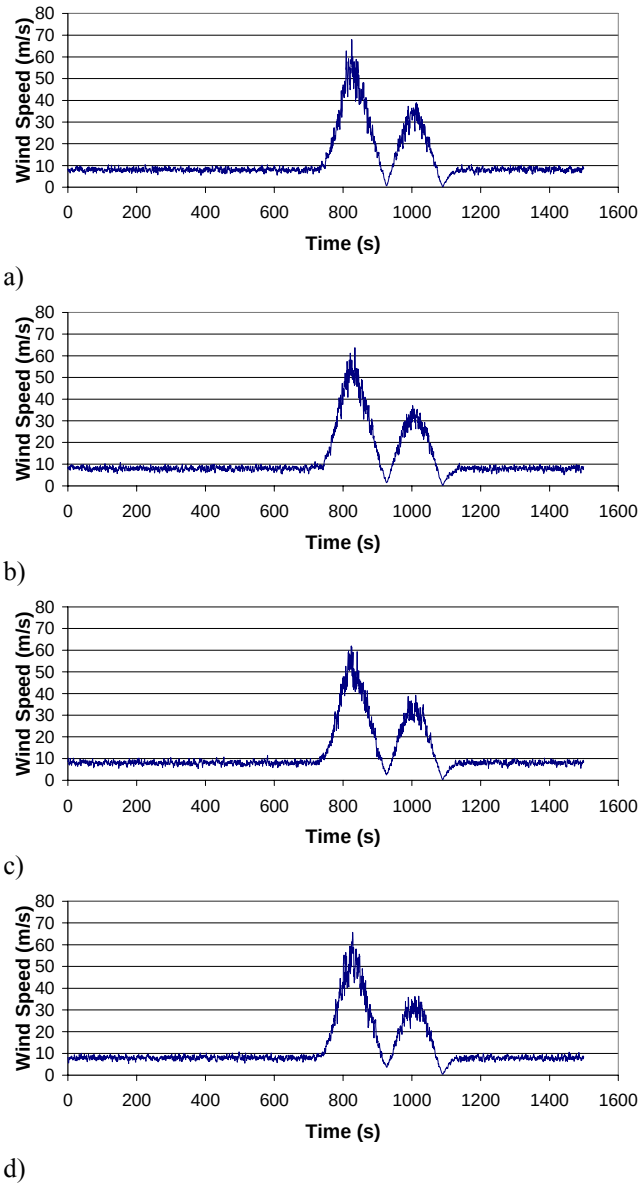

Figure 22: Simultaneously simulated wind speed time histories at varied offsets from the centre-line of the storms path of a) 0m b) 20m c) 40m and d) 60m.

The ability to create simultaneous, correlated wind speed time histories is particularly important for

investigating the response of 'wide' structures, such as transmission lines. The lower turbulence level and higher non-turbulent wind speeds produced during a downburst imply that they will produce a higher, more correlated gust loading on a long span structure than a boundary layer wind.

5.0 Conclusions

Numerous techniques exist for modelling various aspects of a downburst wind field that are relevant to generating a time history of wind loading on a structure. However, little has been done to form an integrated model that includes all of these aspects.

Computational fluid dynamics have been used in this study to simulate the non-turbulent wind speeds of a downburst for a wide range of intensities and sizes, and the basic characteristics of the flows have been examined and compared. The aim was not to develop the accuracy of CFD further, but rather investigate the usefulness of this tool as it stands in its current state. The results demonstrate the effectiveness of CFD for simulating non-turbulent downburst winds, although high-light several short-comings that suggest at this stage other methods may be more effective. Accuracy and versatility should only improve as research continues in this experimental field of fluid mechanics.

A basic analytical model for describing non-turbulent downburst winds was also described. Several modifications to the OBV model (Vicroy 1991) have been suggested, which improve the model's accuracy, useability, and also the ease with which it can be adapted in the future. The changes isolate several key features of the non-turbulent wind field, including:

- radius to maximum wind speed as a function of time
- intensity as a function of time
- the effect of translational speed
- elevation of maximum speed as a function of radius

In most cases simple relationships for these features were suggested. As future research and full-scale observation enables more accurate characterisation of these traits, the current form of the model can be readily adapted to suit changing information.

Finally, turbulence created by an ARMA method is added to the non-turbulent wind speed to form a complete wind speed model for the dynamic analysis of a structure. A full-scale case was simulated, and simultaneous wind speed time histories were created for a set of spaced nodes.

6.0 Acknowledgements

The authors would like to thank Powerlink and Mr. Henry Hawes for supporting this research.

Appendix A

Turbulent fluctuations were created using the Samaras et al (1985) method. Full details of the procedure for applying this method are described in the above reference, but are summarized below for longitudinal turbulence.

The turbulent fluctuations were modelled using a Gaussian stochastic process, $\kappa(x,y,z,t)$, over space (x,y,z) and time (t). $\kappa(x,y,z,t)$ has zero mean, unit variance and is stationary over time.

One approach to representing $\kappa(x,y,z,t)$ is to discretize space and time, and then model $\kappa(x,y,z,t)$ as a vector ARMA process over time, where the components of the vector are the different processes for the spatial locations. For convenience, write $K(t)$ as this vector process so $K(t)=\{\kappa(x,y,z,t)\}_{x,y,z}$. Assuming the order of the moving average and the autoregressive parts of the process are the same (q), the vector ARMA process is then given by

$$\mathrm{K}(t)=\sum_{i=1}^{q} A_i \mathrm{K}(t-i\Delta t)+\sum_{i=0}^{q} B_i \Psi(t-i\Delta t) \qquad \text{(A1)}$$

where $\Psi(t)$ is the vector of white noise at time t and it is assumed that t takes on values $i\Delta t$ where i is an integer.

Given that $K(t)$ is a stationary Gaussian (vector) process over time, only the mean (assumed to be zero) and the covariance structure need to be specified. Thus, as the variances are assumed to be one, the first step is to choose a model for the cross correlation matrix $C_{K(t)}$ between $K(s)$ and $K(s+t)$. The cross correlation matrix is dependent on t, but not s due to the process's stationarity over time. Cross correlations will be modelled assuming time t is continuous. The resulting correlation matrix for $\{K(i\Delta t)\}_i$ (i.e. for the time discretized process) will then be used to determine the coefficient matrices (A_i and B_i) in (A1).

If $K(t)$ has l components (i.e. there are l spatial locations), then the cross-correlation matrix is given by

$$C_{\mathrm{K}}(t)=\begin{bmatrix} P_{11}(t) & P_{12}(t) & \dots & P_{1l}(t) \\ P_{21}(t) & P_{22}(t) & \dots & P_{2l}(t) \\ \dots & \dots & \dots & \dots \\ P_{l1}(t) & P_{2l}(t) & \dots & P_{ll}(t) \end{bmatrix} \qquad \text{(A2)}$$

where $P_{ij}(t)$ is the cross-correlation between the ith and jth locations at times s and $s+t$, respectively, for $i,j=1,2,\dots,l$. If (x_i,y_i,z_i) denotes the ith spatial location, then $P_{ij}(t)$ is assumed to be

$$P_{ij}(t)=\int_0^{\infty}\sqrt{S_i(n)S_j(n)}\,coh\left(y_i,z_i,y_j,z_j,n\right)\cos(2\pi nt)\,dn \qquad \text{(A3)}$$

where $S_i(n)$ is the power spectral density function at location i and $coh(y_i,z_i,y_j,z_j,n)$ is the coherence at frequency n. The correlations given by (A3) are calculated using numerical integration (using Simpson's rule).

The Kaimal spectrum (Kaimal et al 1972) was used as the basis for generating the turbulent fluctuations:

$$\frac{nSi(n)}{u_*^2}=\frac{105f}{(1+33f)^{5/3}} \qquad \text{(A4)}$$

Where u_* is the friction velocity, and

$$f(n,z_i)=\frac{nz_i}{U_{trans}(z_i)} \qquad \text{(A5)}$$

is the reduced frequency.

Spatial coherence was modelled using Davenport's approximation:

$$coh\left(y_i,z_i,y_j,z_j,n\right)=\exp\left[-\hat{f}\left(y_i,z_i,y_j,z_j,n\right)\right] \qquad \text{(A6)}$$

where

$$\hat{f}\left(y_i,z_i,y_j,z_j,n\right)=\frac{n\left[c_z^2\left(z_i-z_j\right)^2+c_y^2\left(y_i-y_j\right)\right]^{1/2}}{\frac{1}{2}\left[U_{trans}\left(z_i\right)+U_{trans}\left(z_j\right)\right]} \qquad \text{(A7)}$$

where the constants c_y and c_z describe the relative effect of separation in the y (lateral) and z (height) directions respectively.

The cross-correlation matrices for each time are then combined to form a complete correlation matrix C for the process $K(t)$:

$$C=\begin{bmatrix} C_{\mathrm{K}}^T(0) & C_{\mathrm{K}}^T(\Delta t) & C_{\mathrm{K}}^T(2\Delta t) & \dots & C_{\mathrm{K}}^T((p-1)\Delta t) \\ C_{\mathrm{K}}(\Delta t) & C_{\mathrm{K}}(0) & C_{\mathrm{K}}^T(\Delta t) & \dots & C_{\mathrm{K}}^T((p-2)\Delta t) \\ C_{\mathrm{K}}(2\Delta t) & C_{\mathrm{K}}(\Delta t) & C_{\mathrm{K}}(0) & \dots & C_{\mathrm{K}}^T((p-3)\Delta t) \\ \dots & \dots & \dots & \dots & \dots \\ C_{\mathrm{K}}((p-1)\Delta t) & C_{\mathrm{K}}((p-2)\Delta t) & C_{\mathrm{K}}((p-3)\Delta t) & \dots & C_{\mathrm{K}}(0) \end{bmatrix} \qquad \text{(A8)}$$

where t takes the values $\{\Delta t,2\Delta t,\dots,p\Delta t\}$ and p denotes the number of time points.

The next step is to use the matrix C to calculate the coefficient matrices in (A1). A set of matrices, $\tilde{A}_i$, are first calculated for $i = 1,\dots,p$, using

$$\begin{bmatrix}\tilde{A}_1 & \tilde{A}_2 & \dots & \tilde{A}_p\end{bmatrix}=-\begin{bmatrix}C_{YY}^T(\Delta t) & C_{YY}^T(2\Delta t) & \dots & C_{YY}^T(p\Delta t)\end{bmatrix}C^{-1} \qquad \text{(A9)}$$

Next, a matrix B_0, which is lower triangular, is obtained using a Cholesky decomposition applied to the solution of:

$$B_0 B_0^T = \sum_{i=0}^{\infty} \widetilde{A}_i C_{\mathrm{K}}(i\Delta t) \qquad \text{(A10)}$$

A matrix D is then constructed:

$$D = \begin{bmatrix} I & \cdots & 0 & -C_{\Psi\mathrm{K}}^T(0) & \cdots & 0 \\ \vdots & \ddots & \vdots & \vdots & \ddots & \vdots \\ 0 & \cdots & I & -C_{\Psi\mathrm{K}}^T((1-q)\Delta t) & \cdots & -C_{\Psi\mathrm{K}}^T(0) \\ -C_{\Psi\mathrm{K}}(0) & \cdots & -C_{\Psi\mathrm{K}}((1-q)\Delta t) & C_{\mathrm{K}}(0) & \cdots & C_{\mathrm{K}}^T((q-1)\Delta t) \\ \vdots & \ddots & \vdots & \vdots & \ddots & \vdots \\ 0 & \cdots & -C_{\Psi\mathrm{K}}(0) & C_{\mathrm{K}}((q-1)\Delta t) & \cdots & C_{\mathrm{K}}(0) \end{bmatrix} \qquad \text{(A10)}$$

where the $C_{\Psi K}$ matrices are calculated from the relationship:

$$C_{\Psi\mathrm{K}}(0) = B_0 \qquad \text{(A11)}$$

and

$$C_{\Psi\mathrm{K}}(-k\Delta t) + \sum_{i=1}^{k} \left(\widetilde{A}_i C_{\Psi\mathrm{K}}((i-k)\Delta t) \right) = 0 \qquad \text{(A12)}$$

for k=1,2,…q, noting that $C_{\Psi K}$ = 0 for a positive time interval.

Finally the coefficient matrices in (A1) are calculated from:

$$\begin{bmatrix} B_1 & B_3 & \ldots & B_q & A_1 & A_2 & \ldots & A_q \end{bmatrix} = \begin{bmatrix} C_{\Psi\mathrm{K}}(-\Delta t) & \ldots & C_{\Psi\mathrm{K}}(-q\Delta t) & -C_{\mathrm{K}}^T(\Delta t) & \ldots & -C_{\mathrm{K}}^T(q\Delta t) \end{bmatrix} D^{-1}$$

(A13)

A vector time series of indefinite length can then be generated using (A1).

The time series generated has a standard deviation of 1, for each time and location. The desired variance is then achieved using amplitude modulation, similar to that outlined by Chen and Letchford (2004a):

$$u'(x,y,z,t) = a(x,y,z,t)\kappa(x,y,z,t) \qquad \text{(A14)}$$

7.0 References

Alahyari, A., and Longmire, E. K. (1995). "Dynamics of Experimentally Simulated Microbursts." *AIAA Journal*, 33(11), 2128-2136.

Brennan, M. (2004). Personal Communication – FLUENT 6.0 boundary conditions. M. Chay, ed., Brisbane, QLD, Australia.

Chang, H.P., and Frost, W. (1987). "Development of a Microburst Turbulence Model for the Joint Airport Weather Studies Wind Shear Data." *NASA-CR-180374*, NASA, Springfield, Virginia.

Chay, M.T. (2001). "Physical Modeling of Thunderstorm Downbursts for Wind Engineering Applications," Masters Thesis, Texas Tech University, Lubbock, TX USA.

Chay, M.T. and Albermani, F. (2004). "A review of downburst wind models for dynamic analysis of lattice structures." *Developments in Mechanics of Structures and Materials: Proceedings of the 18th Australasian Conference on the Mechanics of Structures and Materials*, Vol 1, Perth, Australia, 1-3 Dec 2004, 353-358.

Chay, M.T., and Letchford, C.W. (2002). "Pressure distributions on a cube in a simulated thunderstorm downburst - Part A: stationary downburst observations." *Journal of Wind Engineering and Industrial Aerodynamics*, 90, 711-732.

Chen, L. and Letchford C.W. (2004a) "A deterministic-stochastic hybrid model of downbursts and its impact on a cantilever structure" *Engineering Structures*, 26, 619-626.

Chen, L. and Letchford C.W. (2004b) "Multi-Scale Correlation Analyses of Two Lateral Profiles of Full-Scale Downburst Wind Speeds", *Unpublished*

Choi, E.C.C. (2004). "Field measurement and experimental study of wind speed profile during thunderstorms." *Journal of Wind Engineering and Industrial Aerodynamics*, 92, 275-290.

Cimbala, J.M., Billet, M.L., Gaublomme, D.P. and Oefelein, J.C. (1991), "Experiments on the Unsteadiness Associated with a Ground Vortex," *Journal of Aircraft*, 28- 4, 261-267.

Fluent Inc (2003). FLUENT 6.0. Lebanon, NH, USA.

Fujita, T.T. (1983). "Andrews AFB Microburst." University of Chicago, Chicago, Illinois.

Hangan, H., Roberts, D., Xu, Z., and Kim, J.-D. (2003) "Downburst simulations. Experimental and numerical challenges." *11th International Conference on Wind Engineering*, Lubbock, TX, USA.

Hjelmfelt, M.R. (1988). "Structure and Life Cycle of Microburst Outflows Observed in Colorado." *Journal of Applied Meteorology*, 27, 900-927.

Holmes, J. D., and Oliver, S. E. (2000). "An empirical model of a downburst." *Engineering Structures*, 22, 1167-1172.

Jung-lei, X., Zhong, X., Kun-yuan, Z., and Min, X. (2000). "Numerical Study of Turbulent Impinging Jet With A Refined k-epsilon model." *Journal of Hydrodynamics*, 4, 8-15.

Kaimal, J.C., Wyngaard, J.C., Izumi, Y., and Cote, O.R. (1972). "Spectral Characteristics of surface-layer turbulence." *Quarterly Journal of the Royal Meteorological Society*, 98, 563-589.

Landreth, C.C., and Adrian, R.J. (1990). "Impingement of a low Reynolds number turbulent circular jet onto a flat plate at normal incidence." *Experiments in Fluids*, 9, 74-84.

Lee, B. D. and C. A. Finley (2002). "Fine-scale Outflow Structure of the 10 July 2001 Greeley, CO Convective Wind Event." *21st Conference on Severe Local Storms*, San Antonio TX.

Letchford, C.W., and Chay, M.T. (2002). "Pressure Distributions on a cube in a simulated thunderstorm downburst - Part B: moving downburst observations." *Journal of Wind Engineering and Industrial Aerodynamics*, 90, 733-753.

Letchford, C.W., and Mans, C. (1999). "Physical Modelling of Thunderstorm Downbursts by a Moving Wall Jet." University of Queensland, for Powerlink, Brisbane, Queensland, Australia.

Lundgren, T. S., Yao J., and Mansour, N.N. (1992). "Microburst modelling and scaling." *Journal of Fluid Mechanics*, 239, 461-488.

Mason, M. (2003). "Physical Simulation of Thunderstorm Downbursts," Masters Thesis, Texas Tech University, Lubbock, Texas, USA.

Oliver, S.E., Moriarty, W.W., and Holmes, J.D. (2000). "A risk model for design of transmission line systems against thunderstorm downburst winds." *Engineering Structures*, 22, 1173-1179.

Oseguera, R.M., and Bowles, R.L. (1988). "A simple, analytics 3-dimensional downburst model based on boundary layer stagnation flow." *NASA-TM-100632*, NASA Langley Research Center, Hampton, Virginia.

Qing-guang, C., Zhong, X., and Yong-jian, Z. (2003). "Application of Two Versions of a RNG Based k-epsilon Model to Numerical Simulations of Turbulent Impinging Jet Flow." *Journal of Hydrodynamics*, 2, 71-76.

Samaras, E., Shinozuka, M., and Tsurui, A. (1985). "ARMA Representation of Random Processes." *Journal of Engineering Mechanics*, 111(3), 449-461.

Selvam, R.P., and Holmes, J.D. (1992). "Numerical Simulations of Thunderstorm Downbursts." *Journal of Wind Engineering and Industrial Aerodynamics*, 41-44, 2817-2825.

Simiu, E. and R. H. Scanlan (1996). "*Wind effects on Structures: fundamentals and applications to design.*" 3rd Edition, 688 pages, New York, USA, John Wiley and Sons.

Thielen, L., H. J. J. Jonker, and Hanjalic, K. (2003). "Symmetry breaking of flow and heat transfer in multiple impinging jets." *International Journal of Heat and Fluid Flow*, 24, 444-453.

Vicroy, D.D. (1991). "A Simple, Analytical, Axisymmetric Microburst Model for Downdraft Estimation." *NASA-TM-104053*, N.A.S.A, Hampton, Virginia, USA.

Vicroy, D.D. (1992). "Assessment of Microburst Models for Downdraft Estimation." *Journal of Aircraft*, 29(6), 1043-1048.

Wilson, J.W., Roberts, R.D., Kessinger, C., and McCarthy, J. (1984). "Microburst Wind Structure and Evaluation of Doppler Radar for Airport Wind Shear Detection." *Journal of Climate and Applied Meteorology*, 23(6), 898-915.

Wood, G.S., Kwok, K.C.S., Motteram, N.A., and Fletcher, D.F. (2001). "Physical and numerical modelling of thunderstorm downbursts." *Journal of Wind Engineering and Industrial Aerodynamics*, 89, 532-552.

Yao, J. and T. S. Lundgren (1996). "Experimental investigations of microbursts." *Experiments in Fluids*, 21, 17-25.